Conduction band structure of high-mobility organic semiconductors and partially dressed polaron formation

Haruki Sato[1#], *Syed A. Abd. Rahman*[1#], *Yota Yamada*[1], *Hiroyuki Ishii*[2]*, *Hiroyuki Yoshida*[3,4]*

[1] Graduate School of Science and Engineering, Chiba University, 1-33 Yayoi-cho, Inage-ku, Chiba 263-8522, Japan

[2] Department of Applied Physics, Faculty of Pure and Applied Sciences, University of Tsukuba, 1-1-1 Tennodai, Tsukuba, Ibaraki 305-8573, Japan

[3] Graduate School of Engineering, Chiba University, 1-33 Yayoi-cho, Inage-ku, Chiba 263-8522, Japan

[4] Molecular Chirality Research Center, Chiba University, 1-33 Yayoi-cho, Inage-ku, Chiba 263-8522, Japan

ABSTRACT

The energy band structure provides crucial information on charge transport behaviour in organic semiconductors, such as effective mass, transfer integrals, and electron-phonon coupling. Despite the discovery of the valence (the highest occupied molecular orbital (HOMO)) band structure in 1990s, the conduction band (the lowest unoccupied molecular orbital (LUMO)) has not been experimentally observed. In this work, we employ angle-resolved low-energy inverse photoelectron spectroscopy to reveal the LUMO band structure of pentacene, a prototypical high-mobility organic semiconductor. The derived transfer integrals and bandwidths from the LUMO are substantially smaller than those predicted by density functional theory calculations. To reproduce this bandwidth reduction, we propose an improved (partially dressed) polaron model that accounts for the electron-intramolecular vibrational interaction with frequency-dependent coupling constants based on Debye relaxation. This model quantitatively reproduces not only the transfer integrals, but also the temperature-dependent HOMO and LUMO bandwidths, and the hole and electron mobilities. The present results demonstrate that electron mobility in high mobility organic semiconductors is indeed limited by polaron formation.

*** Corresponding Authors, E-mail: ishii@bk.tsukuba.ac.jp, hyoshida@chiba-u.jp**

 # These authors contributed equally to this work.

Semiconductor devices that use organic materials exhibit unique physical properties such as light weight, printability, and flexibility. These properties originate in the fact that organic semiconductors are composed of molecules bound by weak intermolecular interactions such as van der Waals forces. The weak intermolecular interactions result in unique charge transport mechanisms. Generally, the localized carriers travel incoherently by hopping from one molecule to another in organic semiconductors. Conversely, some organic semiconductors with carrier mobility exceeding ca. 1 $cm^2 V^{-1}s^{-1}$ show band-like transport as evidenced by the temperature-dependent mobility[1], the Hall effect[2–4], electron spin resonance (ESR)[3,5], and ultraviolet photoelectron spectroscopy (UPS)[6]. However, the standard band model developed for conventional semiconductors such as Si, Ge, or GaAs does not adequately describe the charge transport in organic semiconductors because the electron-phonon interaction (this term includes both the hole-phonon and electron-phonon interactions) plays a central role in the charge transport mechanism[7–14].

The electron-phonon interaction affecting the charge transport in an organic semiconductor has been discussed from two perspectives. One is the modulation of the intermolecular electronic coupling (transfer integral) by the intermolecular vibration called the dynamic disorder[15]. The other is the stabilization of the charge carrier by the deformation of the on-site molecule and lattice [16,17]. Such a quasi-particle dressed with the deformation of the molecule and lattice is called a polaron. In organic semiconductors, the energies of the transfer integral, the intramolecular vibration, and the electron-vibration (phonon) coupling constant are around 100 meV, which are comparable and compete with each other. Any subtle changes of these key parameters would cause a drastic change in the appearance of the physical properties. Furthermore, the similarity in magnitude of these energy parameters makes theoretical analysis difficult. Thus, the polaron formation in high-mobility organic semiconductors has been intensely debated[12,18]. The experimental demonstration of the polaron formation is highly awaited.

Experimentally, the polaron formation can be observed as the narrowing of the bandwidth[17]. The temperature dependence of the width of the highest occupied molecular orbital (HOMO)-derived occupied band (referred to as HOMO band, hereinafter) observed by angle-resolved ultraviolet photoelectron spectroscopy (ARUPS) should provide evidence of the polaron formation [19–21]. Unfortunately, an attempt to demonstrate the polaron formation on the basis of the temperature dependence of the HOMO bandwidth [20] failed because the bandwidth is also affected by the thermal expansion of the crystal[22]. So far, the polaron formation has never been experimentally proved.

Because the electron-phonon coupling constants are different between the hole (HOMO) and the electron (lowest unoccupied molecular orbital; LUMO)[23], we anticipate that the different behavior of the HOMO and LUMO bandwidths will provide evidence of the polaron formation. Whereas the HOMO band structure has been examined using energy-dependent UPS or ARUPS since the 1990s[6], the LUMO-derived unoccupied band (LUMO band) structure has never been observed. The unoccupied states can be observed by inverse photoelectron spectroscopy (IPES). The unoccupied LUMO energy of organic materials without momentum resolution has been measured by IPES for more than three decades by several groups[24–29]. To observe the LUMO (conduction) band structure, a set of IPES spectra are measured as a function of the electron incident angle. This experimental method is called angle-resolved inverse photoelectron spectroscopy (ARIPES)[30]. For organic semiconductors, however, even IPES measurements without angular resolution have been very difficult because of serious sample damage owing to electron bombardment. The ARIPES measurement of organic semiconductors is practically impossible because it requires measurements of several to a few tens IPES spectra with varying electron incident angles. In 2012, we invented low-energy inverse photoelectron spectroscopy (LEIPS) to examine the unoccupied levels of organic materials without sample damage[31,32]. Since then, we have been making efforts to realize angular resolution with LEIPS. Our hard work has led to the development of an angle-resolved LEIPS (AR-LEIPS), the schematic diagram of which is shown in Figure S1.

In this work, we report the LUMO band structure of organic semiconductors using AR-LEIPS. We choose the thin-film phase of pentacene[33] as the sample for this study. Pentacene is a prototypical high-mobility organic semiconductor. Among several polymorphs of pentacene, the thin-film phase is extensively studied as an active layer of organic thin-film transistors. Furthermore, both the HOMO and the LUMO of pentacene are composed of π-orbitals and have similar spatial extensions leading to similar HOMO and LUMO band structures[34]. Thus, pentacene is an ideal system to discuss polaron formation from the difference/similarity between HOMO and LUMO. We find that the observed LUMO bandwidth is appreciably narrowed compared with the HOMO bandwidth. To reproduce the observed HOMO and LUMO bandwidths, we propose the "partially dressed" polaron model that accounts for the coupling between the electron and the low-frequency intramolecular vibrational mode.

Conduction (LUMO) band structure

Figure 1(a) shows the AR-LEIPS spectra of a 20-nm-thick pentacene film on SiO_2/Si measured from $\theta = 0°$ to 25°(see Supplementary Information S2 for the film preparation conditions). At electron

incident angle $\theta = 0°$ (corresponding to the Γ-point), the spectrum has a peak at 3.02 eV and a shoulder at 2.60 eV, which is clearly shown in the negative second derivative of the spectrum in Figure 1(b). The crystal structures along the *ab*-plane in the real and reciprocal spaces examined in the present work are shown in Figures 1(c) and (d), respectively. We assigned these two features to the two sub-bands originating from the splitting of the LUMO band owing to the two inequivalent molecules in the unit cell[34]. We then applied this analysis to determine the components indicated by the red bars in Figure 1. From the obtained peak energies, we acquired the LUMO band structure (E-$k_{//}$ dispersion relation), as depicted in Figure 2(a). Electron incident angle θ was transformed into the wavenumber parallel to sample surface $k_{//}$ using the relation $\hbar k_{\parallel} = \sqrt{2mE_k}\sin\theta$, where E_k refers to the kinetic energy of the incident electron.

The pentacene thin-film phase grown on an amorphous SiO_2 surface is polycrystalline with the pentacene crystal uniaxially oriented along the c*-axis[33]. Thus, the observed LUMO bands should be a superposition of the bands measured at various azimuth angles in the ab-plane. However, the observed band structure shows good agreement with the calculated band structure (Figure 2(b))[34], particularly with the band along the Γ-Y direction. This finding seems similar to the ARUPS spectra of azimuthally disordered layered materials where the signal from the high-symmetry point is highlighted[35,36].

We simulated the azimuth-angle integrated AR-LEIPS spectrum of the pentacene thin-film phase for comparison with the experimental result. As the pentacene thin-film phase contains two inequivalent molecules in the unit cell, band structure $E(\mathbf{k})$ is described by the tight-binding model with the transfer integrals between equivalent molecules t_i and those between inequivalent molecules t_j expressed as[34]

$$E(\mathbf{k}) = E_0 + \sum_i t_i \cos(\mathbf{k}\cdot\mathbf{r}_i) \pm \left[\left(2\sum_j t_j \cos(\mathbf{k}\cdot\mathbf{r}_j) \right)^2 + \left(\frac{\Delta}{2} \right)^2 \right]^{1/2}, \qquad (1)$$

where $\mathbf{r}_i$ and $\mathbf{r}_j$ signify the positions of the equivalent and inequivalent sites, respectively. E_0 is the offset energy, and Δ accounts for the difference in energy between the two inequivalent sites. We demonstrated that the band structure of the pentacene thin-film phase can precisely be reproduced by Equation 1 with only the three transfer integrals t_1, t_2, and t_3 in Figure 1(c)[34]. In this work, we first optimized the crystal structure on the basis of density functional theory (DFT)[37] with the vdW-DF2

functional[38] (Supplementary Information S3). Then we calculated bare transfer integrals t_i^0 by the maximally localized Wannier functions (MLWFs)[39] for the crystal structure (Supplementary Information S4). As listed in Table 1, the agreement between the transfer integrals reported in Ref. [34] and the present values calculated by the state-of-the-art method means that the transfer integrals obtained by DFT calculations are not dependent on the calculation method. Using calculated transfer integrals t_1, t_2, and t_3, we simulated the azimuth-angle integrated AR-LEIPS spectrum in Figure 2(b). The band dispersions along the high-symmetry points Γ-X and Γ-Y are indeed highlighted.

Overall, the features of the experimental band structure are well reproduced by this simulation. However, the observed bandwidth is appreciably smaller than that calculated by the DFT. Thus, we attempted to fit the band structure calculated by Equation 1 to the experimental one (see Supplementary Information S5). We optimized the transfer integrals (Figure S5) and simulated azimuth-angle integrated band structure $E(k_{//})$ in Figure 2(a), which excellently reproduced the experimental band structure. From the best-fit result, we obtained the experimental transfer integrals $t_1^{exp} = 25 \pm 5$ meV and $(t_2^{exp} + t_3^{exp}) = 110 \pm 10$ meV. As t_2^{exp} and t_3^{exp} are mutually dependent, it was difficult to determine their values. The obtained transfer integrals are a factor of 0.6 to 0.7 smaller than those calculated by DFT (Table 1). From the Equation 1 and the transfer integrals, we estimated the effective mass for electron m^* to be $2.4 \pm 0.1\ m_0$ along the k_y direction, and $4.6\ m_0$ for the direction averaged value, where m_0 refers to the electron rest mass (see Supplementary Information S6).

Partially dressed polaron model

The LUMO band structure splits into two sub-bands owing to the two inequivalent molecules in the unit cell. Specifically, in the pentacene thin-film phase, the largest energy split emerges at the Γ-point (Figure 2(b)). This means that the total bandwidth can be obtained as the energy split at the Γ-point (Figure 2(a)). In this case, the bandwidth was found to be 440 meV which is a factor of 0.7 smaller than the bandwidth of 620 meV obtained by DFT (Table 1). The inclusion of the GW correction only slightly broadens the bandwidth[40,41], meaning that the DFT calculation accurately accounts for the electronic parts of the intermolecular interactions. Note that the experimental HOMO bandwidth is a factor of 0.8 smaller than that of DFT result (see Supplementary Information S7). As the DFT calculation does not include the electron-phonon interaction, we anticipated that the bandwidth narrowing is due to the electron-phonon interaction. The electron-phonon interaction has been discussed from the stabilization of charge carrier by molecule/lattice deformation (the polaron

model[17,42]) and the modulation of the transfer integral by the intermolecular vibration (the dynamic disorder model[9,12,15,18,43]). The latter predicts not the bandwidth narrowing but the linewidth broadening[18]. Therefore, we calculated the bandwidth narrowing at first using the conventional polaron model[17]. Here we only consider the intramolecular vibrational mode because the intermolecular vibration is too slow to form the polaron, as discussed later. The charge carrier dressed by the intramolecular distortion cloud consequently leads to the renormalization of bare transfer integral t^0 [17]. The renormalized transfer integral is given by

$$t_i^{pol} = t_i^0 exp\left\{-\sum_l (1 + 2N_l)(g_l)^2\right\}, \qquad (2)$$

where N_l and g_l represent the phonon number of the l-th intramolecular vibrational mode with frequency ω_l and the coupling constant given by $g_l = \sqrt{\lambda_l / 2\hbar\omega_l}$, respectively[17]. Renormalization factor t_i^{pol}/t_i^0 is proportional to the narrowing ratio of the polaron bandwidth to the bare bandwidth if the tight-binding approximation is applicable, which is usually the case in organic semiconductors.

In previous studies, only the high-frequency intramolecular vibrational modes (e.g., 1360 cm^{-1}) were taken into account[18,44], and often one mode was calculated to represent these high-frequency modes. This simplification may hold as far as the hole in the HOMO band is concerned. However, the electron (LUMO band) couples with the low-frequency intramolecular vibrational mode at 254 cm^{-1} as shown in Figure 3(a). We reproduced the different HOMO/LUMO renormalization factors (see Table S5) only when we included this low-frequency vibrational mode. We calculated the renormalization factors to be 0.29 for the LUMO band and 0.70 for the HOMO band at 300 K. While the HOMO bandwidth is reasonable, the predicted LUMO transfer integrals (Table 1) and bandwidth (174 meV, Figure 3(c)) are too small compared with the respective experimental values.

The conventional polaron model (Eq. 2) assumes that the vibrational period $(\omega_l)^{-1}$ is sufficiently shorter than the movement of the charge carrier (Bloch-wave formation time h/t^0). Actually, the period of high-frequency molecular-vibrational modes around 1360 cm^{-1} is ca. 20 fs, which is shorter than the Bloch-wave formation time of 50 to 100 fs. In contrast, the vibrational period of 130 fs for the low-frequency mode at 254 cm^{-1} is comparable to the Bloch-wave formation time. This means that the molecular motion of the low-frequency mode is too slow to fully dress the charge carrier and should only partially affect the polaron formation. We call this polaron where the charge carrier is interacting

with the molecule in the middle of deformation toward the stable ionic structure, the "partially dressed polaron". To account for the partially dressed polaron formation, we employed the formula generally used to describe the frequency-dependent dielectric response (see Supplementary Information S8 for details). Equation 2 is modified as,

$$t_i^{pol} = t_i^0 exp\left\{-\sum_l (1+2N_l)F(t_i^0, \hbar\omega_l)(g_l)^2\right\}, \qquad (3a)$$

$$F(t_i^0, \hbar\omega_l) = 1 - \frac{1}{1+\left(\frac{\hbar\omega_l}{t_i^0}\right)^2} \quad . \qquad (3b)$$

Function F accounts for the reduction of the renormalization owing to the partial polaron formation. As shown in Figure 3(b), F depends on intramolecular vibrational period $(\omega_l)^{-1}$ and Bloch-wave formation time h/t^0, which are obtained by the first-principles calculations, meaning that this model contains no adjustable parameters. The high-frequency vibrational mode at 1370 cm^{-1} almost entirely contributes to the renormalization with $F = 0.9$, whereas the low-frequency vibrational mode ω_l of 254 cm^{-1} contributes only with $F = 0.3$ when we assume $t_i^0 = 50$ meV. Although we consider only the electron-intramolecular vibration here, this concept can easily be extended to the intermolecular vibration[17]. The frequency of the intermolecular vibration is typically lower than 100 cm^{-1}. The contribution of these vibrational modes to the polaron formation is negligible, e.g., $F = 0.06$ at 100 cm^{-1} for $t_i^0 = 50$ meV.

Using the partially dressed polaron model expressed by Equation 3, we computed renormalized transfer integrals t_i^{pol} at 300 K. The results listed in Table 1 show excellent agreement with the experimental values. Then, assuming the tight-binding approximation (Eq. 1), we calculated the polaron band structures (Figure 3(c)). The polaron transfer integrals of HOMO and LUMO at different temperatures are given in Supplementary Information S9. The bare bandwidths are narrowed by the factors of 0.68 for the LUMO band and 0.78 for the HOMO band. These values are in excellent agreement with the experimental results (Table S5).

Temperature dependence of HOMO and LUMO bandwidths

In order to confirm the validity of our partially dressed polaron model, we examined the temperature dependence of the HOMO and LUMO bandwidths by cooling the sample from the room temperature to approximately 100 K. As we have seen above (Figure 3(a)), the electron (anion) couples with the low-frequency vibrational mode of 254 cm^{-1} (≈30 meV), which is comparable to the thermal energy (26 meV at 300 K) leading to the temperature dependence of the LUMO bandwidth. Conversely, as the hole (cation) only couples with the high-frequency vibrational modes (mostly above 1200 cm^{-1} ≈ 150 meV, much higher than the thermal energy), the HOMO bandwidth is not expected to be affected by the cooling from room temperature.

Figure 4(a) shows the temperature-dependent UPS and LEIPS spectra of the HOMO and LUMO regions at the Γ point. As we have discussed above, the energy difference of the two split components coincides with the (total) bandwidth in the case of the pentacene thin-film phase. The bandwidths of HOMO and LUMO as a function of temperature are shown in Figure 4(b). The LUMO bandwidth increases at low temperatures with the slope of -0.14 ± 0.12 meV K^{-1}, whereas the HOMO bandwidth is independent of the temperature (0.053 ± 0.054 meV K^{-1}). The observed values are in quantitative agreement with the respective calculated results on the basis of our partially dressed polaron model (Eq. 3) for LUMO of -0.139 meV K^{-1} and HOMO of -0.014 meV K^{-1} in the temperature range of 75 and 340 K (Figure 3(d)).

The experimental bandwidth may also be affected by the thermal expansion of the crystalline film. The thermal expansion changes the intermolecular distance, and this change in intermolecular distance affects the magnitude of the intermolecular electronic coupling (i.e., the transfer integrals). However, the calculated bare bandwidths (i.e., without including the polaron effect) based on the thermal expansion coefficients of the 200-nm-thick film[45] predict a large temperature-dependent broadening of approximately -0.2 meV K^{-1} (Figure S8). This is likely because the thermal expansion of the pentacene thin film (10 nm) is restricted by the small thermal expansion of the SiO_2/Si substrate (approximately 2×10^{-6} K^{-1}) [45]. To confirm this hypothesis, we performed another set of temperature-dependent experiments on pentacene film prepared on a Cu(110) substrate[46] whose thermal coefficient (16×10^{-6} K^{-1}) is one order of magnitude larger than that of SiO_2/Si, but is still smaller than that of thick pentacene film (31×10^{-6} and 55×10^{-6} K^{-1} along the *a* and *b* axes, respectively[45]). From the UPS and LEIPS spectra of pentacene/Cu(110) (Figure 4(c)), we determined the temperature dependence of

the bandwidths of HOMO and LUMO (Figure 4(d)) to be -0.24 ± 0.11 meV K^{-1} for LUMO and -0.07 ± 0.04 meV K^{-1} for HOMO. The slightly larger broadening of the HOMO and LUMO bandwidths reflects the larger thermal coefficients of Cu(110) than SiO_2/Si. We conclude that the bandwidths of the present case are little affected by the thermal expansion.

Charge transport and mobility

The polaron formation has direct relevance to the charge transport. It has been reported that the observed electron mobility is one order of magnitude smaller than the hole mobility in the pentacene thin-film phase[47–49] (e.g., electron mobility of 0.01 cm^2/Vs and hole mobility of 0.11 cm^2/Vs at room temperature[50]). However, the band model predicts the similar hole and electron mobilities from the effective masses m^* of the hole (-3.31 m_0) and the electron (3.16 m_0) [34]. This means that the electron-phonon interaction plays a central role in the difference in the hole and electron mobilities.

In previous studies of the charge transport, the modulation of the transfer integral by thermally excited intermolecular vibrations (dynamic disorder) has mainly been discussed[12,15,51], whereas the effect of the polaron on the charge transport seems to be ignored. Here, we calculated the electron and hole mobilities of the pentacene thin-film phase, taking the effect of intramolecular vibrations on both the partially dressed polaron and the dynamic disorder in on-site energies into consideration. For this purpose, we used the time-dependent wave packet diffusion (TD-WPD) method[51,52] and evaluated the mobilities in terms of a time-dependent expression in the Kubo formula using wave packet dynamics (see Supplementary Information S12).

Figure 5 shows the calculated electron and hole mobilities along the *a*-axis (see Fig. 1(c)) as a function of temperature. Both the hole and electron mobilities decrease as the temperature is increased, and this tendency is usually regarded as an indication of band-like transport. When we include only the effect of dynamic disorder on the transfer integrals as in previous studies[12,15,51,53], the mobilities at 300 K are 7.83 cm^2/Vs for the bare electron and 22.1 cm^2/Vs for the bare hole. The ratio of bare hole and electron mobilities is only 2.8, which is too small compared with the experimental values. When we take the intramolecular vibration effects including the partially dressed polaron formation and the dynamic disorder of the on-site energies into account based on Equation 3, the electron mobility is reduced to 1.4 cm^2/Vs whereas the hole mobility is moderately decreased to 15.6 cm^2/Vs at 300 K. The calculated result including the partially dressed polaron excellently explains the one order of

magnitude difference between the hole and electron mobilities measured for the pentacene thin-film field-effect transistors.

Outlook

In this study, we directly observed the LUMO-derived conduction band of organic semiconductors by means of AR-LEIPS. We adopted a uniaxially oriented thin film of pentacene as the sample because of the large band dispersion, the similarity between the calculated HOMO and LUMO band structures and the relevance to field effect transistor application. By comparing the experimental and simulated band structures for the azimuthally disordered crystal, we determined the experimental transfer integrals to be $t_1^{exp} = 25$ meV and $(t_2^{exp} + t_3^{exp}) = 110$ meV in the framework of the tight-binding model. We also determined that electron effective mass m^*/m_0 was 2.4 ± 0.1.

We observed appreciable narrowing of the LUMO bandwidth compared with the HOMO bandwidth, which was analyzed by the renormalization of the transfer integrals owing to the polaron formation. We found that the coupling between the electron (LUMO) and the low-frequency vibrational mode of 254 cm^{-1} is crucial to understanding the LUMO bandwidth narrowing. To take into account the "partial coupling" between a charge and a low-frequency vibrational mode due to the slow molecular motion relative to the charge motion, we proposed a "partially dressed" polaron model with the frequency-dependent reducing factor (Eq. 3b) based on the Debye relaxation. This model is able to quantitatively explain not only the observed HOMO and LUMO bandwidth narrowing but also the temperature dependence of the HOMO and LUMO bandwidths. In addition, our calculated hole and electron mobilities excellently reproduce the difference of one order of magnitude between the experimental hole and electron mobilities. We would like to stress that our partially dressed polaron model has no adjustable parameters; all the parameters are taken from the first-principles calculations.

The present results establish the polaron formation in high-mobility organic semiconductors. The fact that only the electron couples with the low-frequency vibrational mode seems to be common nature in polyacene molecules[23]. Further study is under way to elucidate the origin of the inferiority of the electron mobility to the hole mobility based on our partially dressed polaron model.

AUTHOR INFORMATION

Corresponding Authors

*E-mail addresses: ishii@bk.tsukuba.ac.jp; hyoshida@chiba-u.jp

ACKNOWLEDGMENTS

The authors thank Professor Nobuo Ueno for stimulating and helpful discussion on the electron-phonon coupling of organic semiconductors. This work was supported by JSPS KAKENHI (26288007, JP18H01856, 21H01902, and 21H05472), JST PRESTO, CREST (JPMJCR21Q1), and the Futaba Research Grant Program of the Futaba Foundation. S.T. thanks the JST SPRING grant (JPMJSP2109) for financial support. H.I. also acknowledges the financial support from the University of Tsukuba, Pre-Strategic Initiatives "Development Center for High-Function and High-Performance Organic-Inorganic Spin Electronics".

AUTHOR CONTRIBUTIONS

H. Y. created the concept of this work. H.S., S.A.A.R., and Y.Y. made the acquisition and analysis of the experimental data. H.I. and H.Y. performed the theoretical analysis. H.S. and H.Y. wrote the manuscript.

COMPETING INTERESTS

The authors declare no competing interests.

ORCID

Hiroyuki Ishii: 0000-0003-0644-1424

Hiroyuki Yoshida: 0000-0002-8889-324X

DATA AVAILABILITY

All the data supporting the findings of this study are available within the article, its Supplementary Information files, or from the corresponding authors upon request.

CODE AVAILABILITY

The electronic-state-calculation codes used in this paper are Quantum ESPRESSO, Wannier90 and GAMESS. The Detailed information related to the license and user guide for these codes are

available at https://www.quantum-espresso.org/, http://www.wannier.org/ and https://www.msg.chem.iastate.edu/gamess/.

Table 1. Summary of transfer integrals for the LUMO band (meV).

	Experiment (present work)	**Calculation**			
		DFT-PBE (Ref. [34]) bare t_i^0	bare t_i^0 (present work)	conventional polaron t_i^{pol} at 300 K (Eq. 2)	partially dresssed polaron t_i^{pol} at 300 K (Eq. 3)
t_1	25 ±5	44	46.8	13.1	26.1
t_2	-	73	73.7	20.7	49.7
t_3	-	80	81.3	22.8	56.6
$t_2 + t_3$	110 ±10	153	155.0	43.5	106.3
total bandwidth	440	613	620	174	425

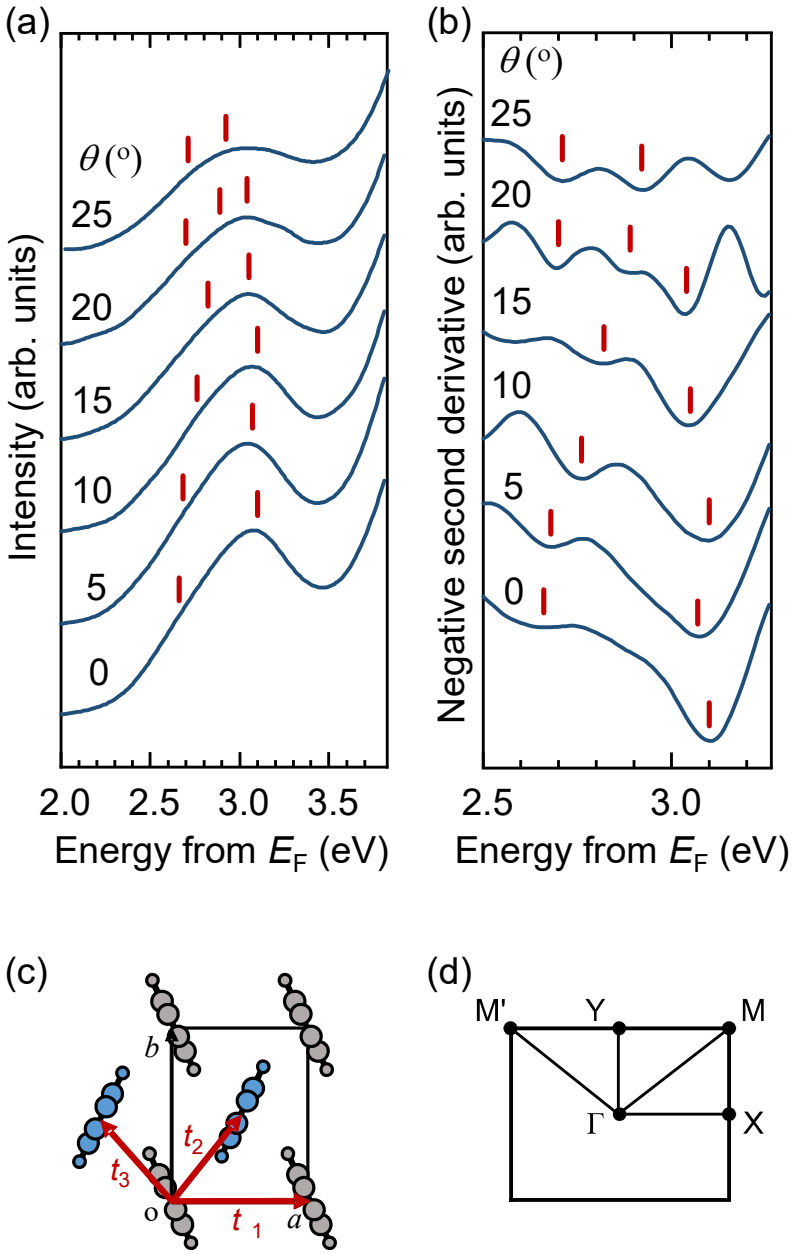

Figure 1. AR-LEIPS spectra of pentacene thin-film phase on SiO_2. (a) Observed AR-LEIPS spectra and (b) negative second derivatives to distinguish the spectral components as the minima. The peaks are indicated by red bars. (c) Unit cell and molecular arrangement along the *ab*-plane. The three dominant intermolecular interactions are indicated by red arrows with transfer integral t_i. Equivalent and inequivalent molecules are distinguished by gray and blue colors. (d) Brillouin zone along the *ab*-plane examined in this work.

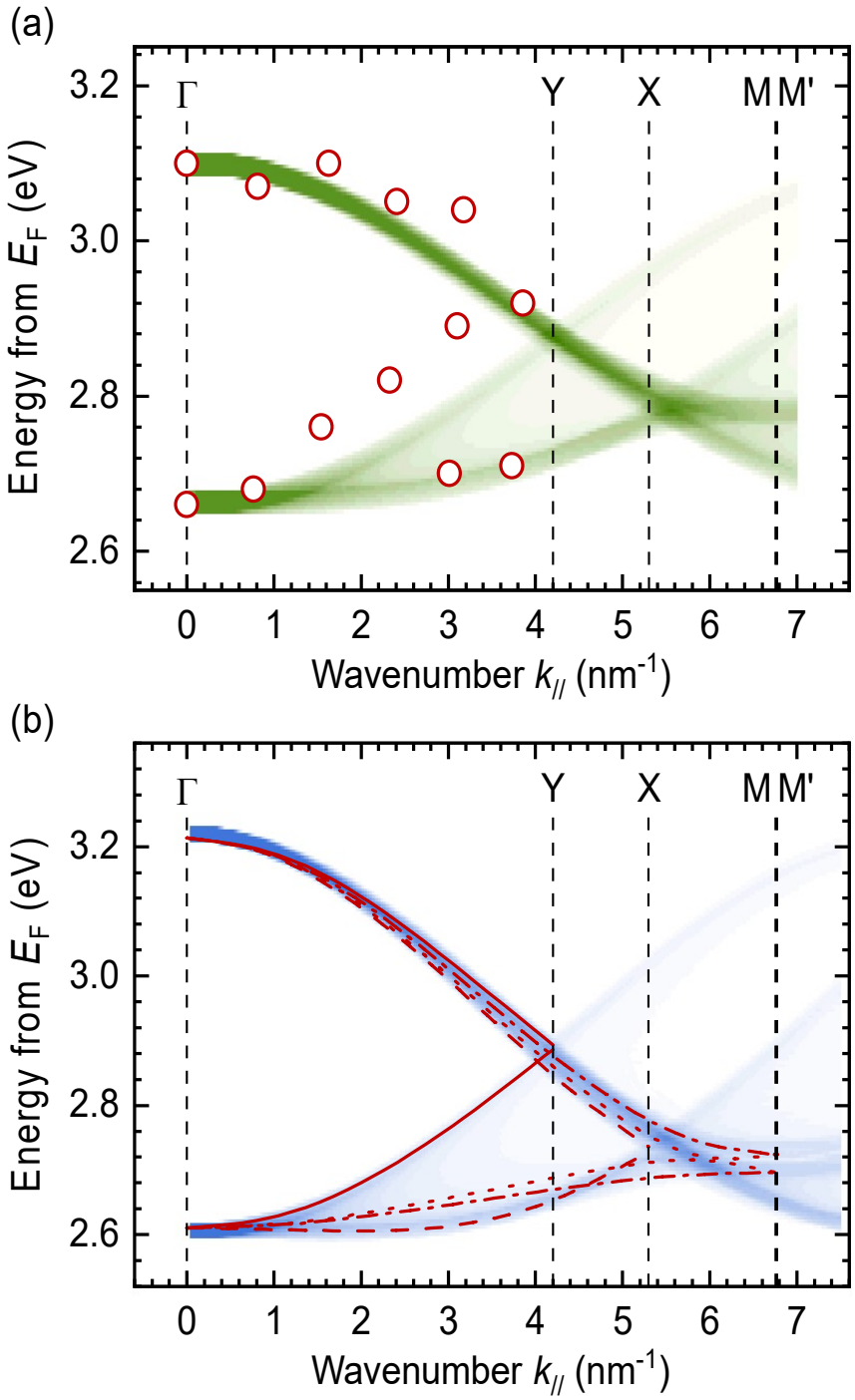

Figure 2. LUMO band structures of pentacene. (a) Experimentally observed LUMO band structure by AR-LEIPS (red open circles). The heatmap in green shows the best-fit results of the simulated azimuth-angle integrated band structure based on Eq. 1. (b) Calculated band structures by DFT (GGA-PBE)[34]. Red lines show the bands along *Γ*-*X* (dashed lines), *Γ*-*Y* (solid lines), *Γ*-*M* (dotted lines), and *Γ*-*M*' (dashed-dotted lines) directions, and the blue shaded area shows the azimuth-angle integrated band structure.

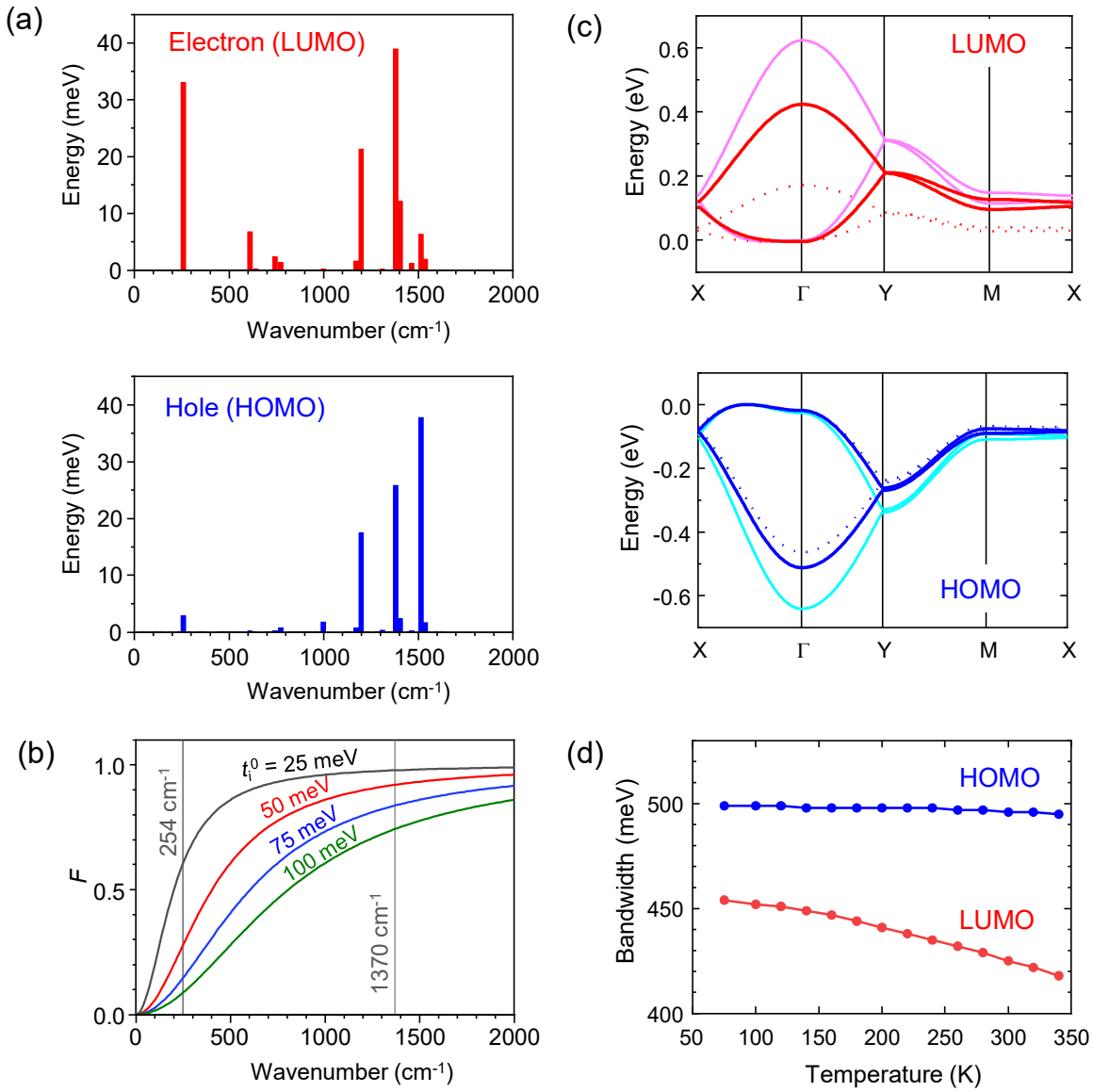

Figure 3. Results of theoretical calculations. (a) Reorganization energies λ_l as a function of intramolecular vibrational frequencies ω_l for the electron (LUMO) and the hole (HOMO). (b) Vibrational frequency dependence of reduction factor F calculated by Equation 3b for different bare transfer integrals t_i^0. (c) Polaron band structures at 300 K calculated on the basis of the conventional polaron model shown by Equation 2 (dotted lines) and the partially dressed polaron model shown by Equation 3 (dark lines). The bare band structures are also shown (light lines). The origin of the energy axis is set to the LUMO band bottom and the HOMO band top, respectively. (d) Temperature dependence of the HOMO and LUMO polaron bandwidths.

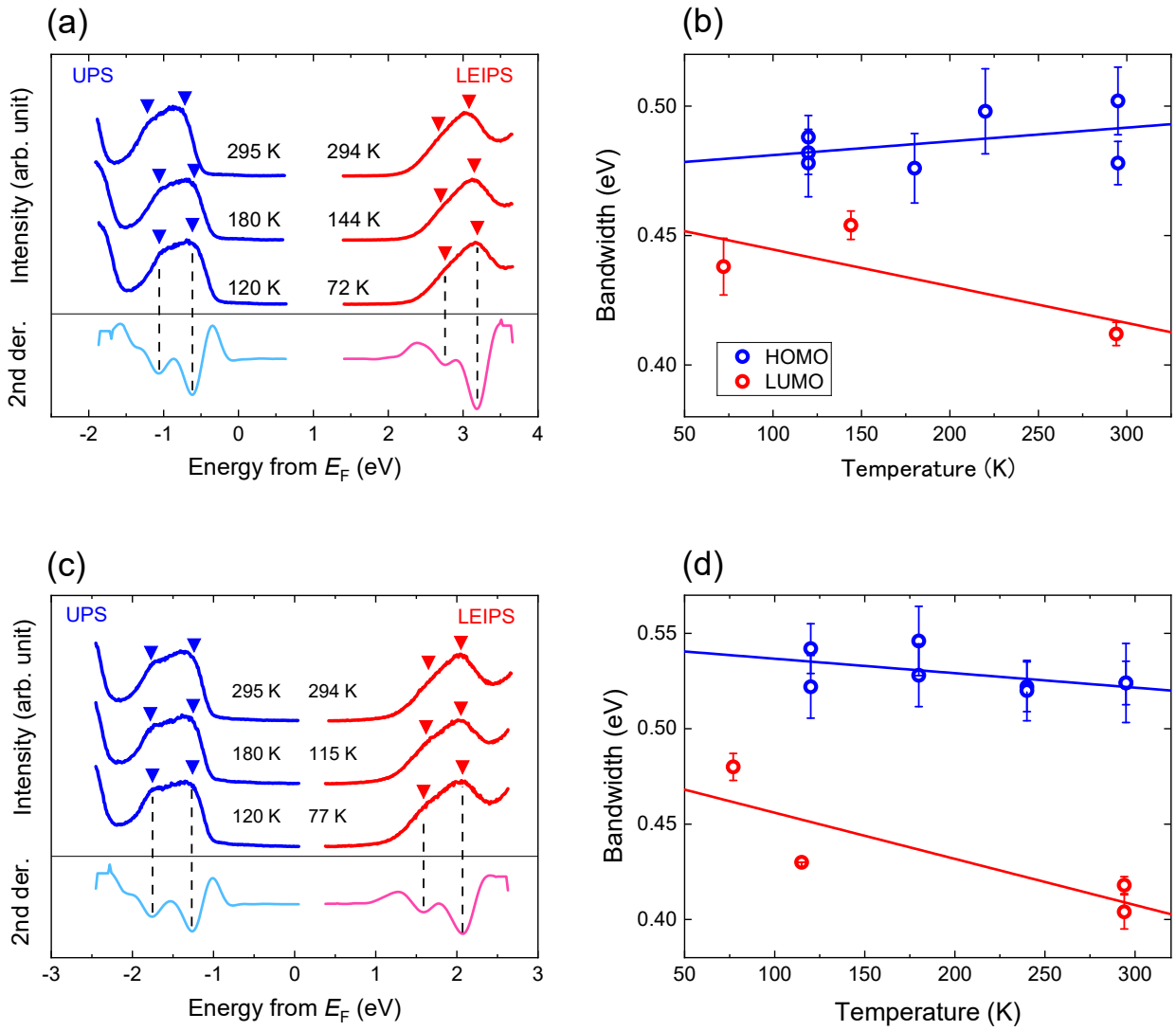

Figure 4. Temperature-dependent UPS and LEIPS spectra. (a) UPS and LEIPS spectra measured in the temperature range of 72 to 295 K. (b) Temperature dependence of experimental HOMO and LUMO bandwidths for pentacene/SiO_2. The temperature dependence is in good agreement with the calculated results shown in Figure 3(d). Panels (c) and (d) show respective data for pentacene/Cu(110). Triangles in panels (a) and (c) indicate the positions of the sub-bands derived from the negative peaks of the second derivatives. The uncertainties are derived from the dependence of the data points used for calculating the 2nd derivatives (see Supplementary Information S11).

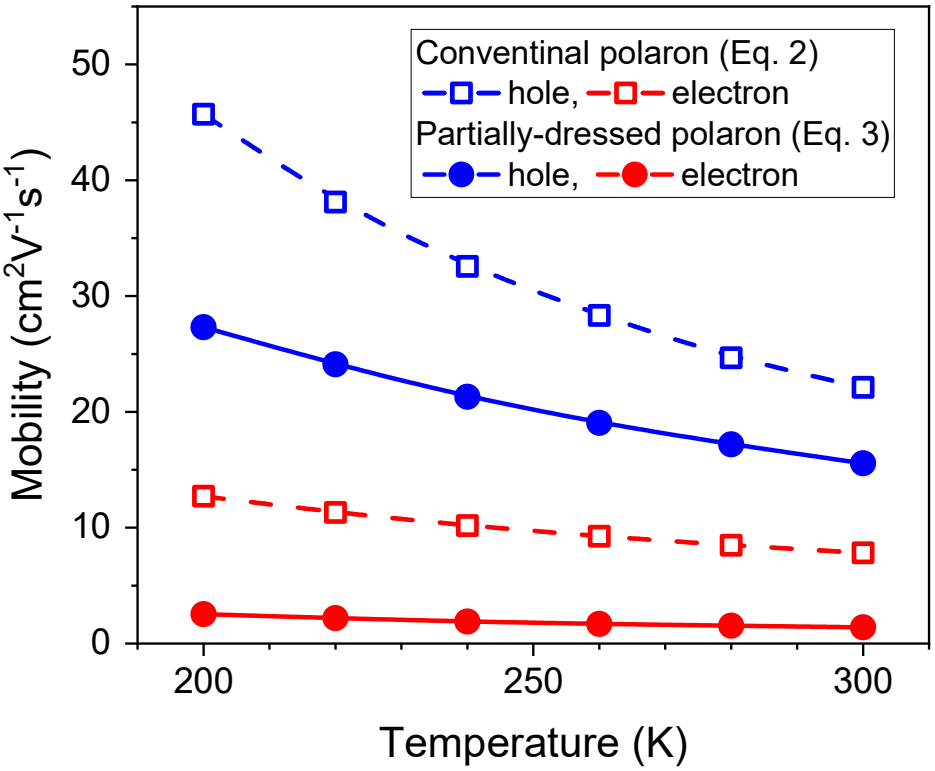

Figure 5. Calculated temperature dependence of electron (red) and hole (blue) mobilities for the pentacene thin-film phase.

FIGURE CAPTIONS

Figure 1. AR-LEIPS spectra of pentacene thin-film phase on SiO_2. (a) Observed AR-LEIPS spectra and (b) negative second derivatives to distinguish the spectral components as the minima. The peaks are indicated by red bars. (c) Unit cell and molecular arrangement along the *ab*-plane. The three dominant intermolecular interactions are indicated by red arrows with transfer integral t_i. Equivalent and inequivalent molecules are distinguished by gray and blue colors. (d) Brillouin zone along the *ab*-plane examined in this work.

Figure 2. LUMO band structures of pentacene. (a) Experimentally observed LUMO band structure by AR-LEIPS (red open circles). The heatmap in green shows the best-fit results of the simulated azimuth-angle integrated band structure based on Eq. 1. (b) Calculated band structures by DFT (GGA-PBE)[34]. Red lines show the bands along *Γ*-*X* (dashed lines), *Γ*-*Y* (solid lines), *Γ*-*M* (dotted lines), and *Γ*-*M*' (dashed-dotted lines) directions, and the blue shaded area shows the azimuth-angle integrated band structure.

Figure 3. Results of theoretical calculations. (a) Reorganization energies λ_l as a function of intramolecular vibrational frequencies ω_l for the electron (LUMO) and the hole (HOMO). (b) Vibrational frequency dependence of reduction factor *F* calculated by Equation 3b for different bare transfer integrals t_i^0. (c) Polaron band structures at 300 K calculated on the basis of the conventional polaron model shown by Equation 2 (dotted lines) and the partially dressed polaron model shown by Equation 3 (dark lines). The bare band structures are also shown (light lines). The origin of the energy axis is set to the LUMO band bottom and the HOMO band top, respectively. (d) Temperature dependence of the HOMO and LUMO polaron bandwidths.

Figure 4. Temperature-dependent UPS and LEIPS spectra. (a) UPS and LEIPS spectra measured in the temperature range of 72 to 295 K. (b) Temperature dependence of experimental HOMO and LUMO bandwidths for pentacene/SiO_2. The temperature dependence is in good agreement with the calculated results shown in Figure 3(d). Panels (c) and (d) show respective data for pentacene/Cu(110). Triangles in panels (a) and (c) indicate the positions of the sub-bands derived from the negative peaks of the second derivatives. The uncertainties are derived from the dependence of the data points used for calculating the 2nd derivatives (see Supplementary Information S11).

Figure 5. Calculated temperature dependence of electron (red) and hole (blue) mobilities for the pentacene thin-film phase.

REFERENCES

1. Karl, N. Charge carrier transport in organic semiconductors. *Synth. Met.* **133**–**134**, 649–657 (2003).

2. Podzorov, V., Menard, E., Rogers, J. A. & Gershenson, M. E. Hall effect in the accumulation layers on the surface of organic semiconductors. *Phys. Rev. Lett.* **95**, 226601 (2005).

3. Hasegawa, T. & Takeya, J. Organic field-effect transistors using single crystals. *Sci. Technol. Adv. Mater.* **10**, 024314 (2009).

4. Lin, Y. J., Tsao, H. Y. & Liu, D. S. Hall-effect mobility of pentacene films prepared by the thermal evaporating method with different substrate temperature. *Appl. Phys. Lett.* **101**, 013302 (2012).

5. Marumoto, K., Kuroda, S. I., Takenobu, T. & Iwasa, Y. Spatial extent of wave functions of gate-induced hole carriers in pentacene field-effect devices as investigated by electron spin resonance. *Phys. Rev. Lett.* **97**, 256603 (2006).

6. Ueno, N. & Kera, S. Electron spectroscopy of functional organic thin films: Deep insights into valence electronic structure in relation to charge transport property. *Prog. Surf. Sci.* **83**, 490–557 (2008).

7. Martinelli, N. G. *et al.* Influence of intermolecular vibrations on the electronic coupling in organic semiconductors: the case of anthracene and perfluoropentacene. *ChemPhysChem* **10**, 2265–2273 (2009).

8. Gershenson, M. E., Podzorov, V. & Morpurgo, A. F. Colloquium: Electronic transport in single-crystal organic transistors. *Rev. Mod. Phys.* **78**, 973–989 (2006).

9. Nematiaram, T. & Troisi, A. Modeling charge transport in high-mobility molecular semiconductors: Balancing electronic structure and quantum dynamics methods with the help of experiments. *J. Chem. Phys.* **152**, 190902 (2020).

10. Schweicher, G. *et al.* Molecular Semiconductors for Logic Operations: Dead-End or Bright Future? *Adv. Mater.* **32**, 1905909 (2020).

11. Schweicher, G., Olivier, Y., Lemaur, V. & Geerts, Y. H. What currently limits charge carrier mobility in crystals of molecular semiconductors? *Isr. J. Chem.* **54**, 595–620 (2014).

12. Fratini, S., Mayou, D. & Ciuchi, S. The transient localization scenario for charge transport in crystalline organic materials. *Adv. Funct. Mater.* **26**, 2292–2315 (2016).

13. Liu, C. *et al.* A unified understanding of charge transport in organic semiconductors: The importance of attenuated delocalization for the carriers. *Mater. Horiz.* **4**, 608–618 (2017).

14. Oberhofer, H., Reuter, K. & Blumberger, J. Charge Transport in Molecular Materials: An Assessment of Computational Methods. *Chem. Rev.* **117**, 10319–10357 (2017).

15. Troisi, A. & Orlandi, G. Charge-transport regime of crystalline organic semiconductors: Diffusion limited by thermal off-diagonal electronic disorder. *Phys. Rev. Lett.* **96**, 086601 (2006).

16. Holstein, T. Studies of polaron motion. Part II. The 'small' polaron. *Ann. Phys. (N. Y).* **8**, 343–389 (1959).

17. Hannewald, K. *et al.* Theory of polaron bandwidth narrowing in organic molecular crystals. *Phys. Rev. B* **69**, 075211 (2004).

18. Ciuchi, S. & Fratini, S. Band dispersion and electronic lifetimes in crystalline organic semiconductors. *Phys. Rev. Lett.* **106**, 166403 (2011).

19. Koch, N. *et al.* Evidence for temperature-dependent electron band dispersion in pentacene. *Phys. Rev. Lett.* **96**, 156803 (2006).

20. Hatch, R. C., Huber, D. L. & Höchst, H. Electron-phonon coupling in crystalline pentacene films. *Phys. Rev. Lett.* **104**, 047601 (2010).

21. Nakayama, Y. *et al.* Single-Crystal Pentacene Valence-Band Dispersion and Its Temperature Dependence. *J. Phys. Chem. Lett.* **8**, 1259–1264 (2017).

22. Li, Y., Coropceanu, V. & Brédas, J. L. Thermal narrowing of the electronic bandwidths in organic molecular semiconductors: Impact of the crystal thermal expansion. *J. Phys. Chem. Lett.* **3**, 3325–3329 (2012).

23. Coropceanu, V. *et al.* Charge transport in organic semiconductors. *Chem. Rev.* **107**, 926–952 (2007).

24. Frank, K. H., Yannoulis, P., Dudde, R. & Koch, E. E. Unoccupied molecular orbitals of aromatic hydrocarbons adsorbed on Ag(111). *J. Chem. Phys.* **89**, 7569–7576 (1988).

25. Hill, I. G. *et al.* Occupied and unoccupied electronic levels in organic π-conjugated molecules: Comparison between experiment and theory. *Chem. Phys. Lett.* **317**, 444–450 (2000).

26. Yoshida, H., Tsutsumi, K. & Sato, N. Unoccupied electronic states of 3d-transition metal phthalocyanines (MPc: M=Mn, Fe, Co, Ni, Cu and Zn) studied by inverse photoemission spectroscopy. *J. Electron Spectros. Relat. Phenom.* **121**, 83–91 (2001).

27. Zahn, D. R. T., Gavrila, G. N. & Gorgoi, M. The transport gap of organic semiconductors studied using the combination of direct and inverse photoemission. *Chem. Phys.* **325**, 99–112 (2006).

28. Krause, S., Casu, M. B., Schöll, A. & Umbach, E. Determination of transport levels of organic semiconductors by UPS and IPS. *New J. Phys.* **10**, 085001 (2008).

29. Kanai, K. *et al.* Determination of electron affinity of electron accepting molecules. *Appl. Phys. A: Mater. Sci. Process.* **95**, 309–313 (2009).

30. Dose, V. Momentum-resolved inverse photoemission. *Surf. Sci. Rep.* **5**, 337–378 (1985).

31. Yoshida, H. Near-ultraviolet inverse photoemission spectroscopy using ultra-low energy electrons. *Chem. Phys. Lett.* **539**–**540**, 180–185 (2012).

32. Yoshida, H. Principle and application of low energy inverse photoemission spectroscopy: A new method for measuring unoccupied states of organic semiconductors. *J. Electron Spectros. Relat. Phenom.* **204**, 116–124 (2015).

33. Yoshida, H., Inaba, K. & Sato, N. X-ray diffraction reciprocal space mapping study of the thin film phase of pentacene. *Appl. Phys. Lett.* **90**, 181930 (2007).

34. Yoshida, H. & Sato, N. Crystallographic and electronic structures of three different polymorphs of pentacene. *Phys. Rev. B* **77**, 235205 (2008).

35. Zhou, S. Y. *et al.* Coexistence of sharp quasiparticle dispersions and disorder features in graphite. *Phys. Rev. B* **71**, 161403 (2005).

36. Park, S. *et al.* Electronic band dispersion determination in azimuthally disordered transition-metal dichalcogenide monolayers. *Commun. Phys.* **2**, 68 (2019).

37. Giannozzi, P. *et al.* QUANTUM ESPRESSO: A modular and open-source software project for quantum simulations of materials. *J. Phys. Condens. Matter* **21**, 395502 (2009).

38. Berland, K. *et al.* van der Waals forces in density functional theory: a review of the vdW-DF method. *Rep. Prog. Phys.* **78**, 066501 (2015).

39. Mostofi, A. A. *et al.* wannier90: A tool for obtaining maximally-localised Wannier functions. *Comput. Phys. Commun.* **178**, 685–699 (2008).

40. Tiago, M. L. *et al.* Ab initio calculation of the electronic and optical properties of solid pentacene. *Phys. Rev. B* **67**, 115212 (2003).

41. Yanagisawa, S. & Hamada, I. Determination of geometric and electronic structures of organic crystals from first principles: Role of the molecular configuration on the electronic structure. *J. Appl. Phys.* **121**, 45501 (2017).

42. Ortmann, F., Bechstedt, F. & Hannewald, K. Theory of charge transport in organic crystals: Beyond Holstein's small-polaron model. *Phys. Rev. B* **79**, 235206 (2009).

43. Fratini, S. & Ciuchi, S. Dynamical localization corrections to band transport. *Phys. Rev. Res.* **2**, 13001 (2020).

44. Houili, H., Picon, J. D., Zuppiroli, L. & Bussac, M. N. Polarization effects in the channel of an organic field-effect transistor. *J. Appl. Phys.* **100**, 23702 (2006).

45. Von Helden, L., Breuer, T. & Witte, G. Anisotropic thermal expansion in pentacene and perfluoropentacene: Effects of molecular packing motif and fixation at the interface. *Appl. Phys. Lett.* **110**, 141904 (2017).

46. Lukas, S., Söhnchen, S., Witte, G. & Wöll, C. Epitaxial growth of pentacene films on metal surfaces. *ChemPhysChem* **5**, 266–270 (2004).

47. Yasuda, T., Goto, T., Fujita, K. & Tsutsui, T. Ambipolar pentacene field-effect transistors with calcium source-drain electrodes. *Appl. Phys. Lett.* **85**, 2098–2100 (2004).

48. Chua, L. L. *et al.* General observation of n-type field-effect behaviour in organic semiconductors. *Nature* **434**, 194–199 (2005).

49. Chiu, L. Y. *et al.* Manipulating the ambipolar characteristics of pentacene-based field-effect transistors. *J. Mater. Chem. C* **2**, 1823–1829 (2014).

50. Saudari, S. R. & Kagan, C. R. Electron and hole transport in ambipolar, thin film pentacene transistors. *J. Appl. Phys.* **117**, 035501 (2015).

51. Ishii, H., Inoue, J. I., Kobayashi, N. & Hirose, K. Quantitative mobility evaluation of organic semiconductors using quantum dynamics based on density functional theory. *Phys. Rev. B* **98**, 235422 (2018).

52. Ishii, H., Kobayashi, N. & Hirose, K. Order- N electron transport calculations from ballistic to diffusive regimes by a time-dependent wave-packet diffusion method: Application to transport properties of carbon nanotubes. *Phys. Rev. B* **82**, 085435 (2010).

53. Fratini, S. *et al.* A map of high-mobility molecular semiconductors. *Nat. Mater.* **16**, 998–1002 (2017).

Methods

Sample Preparation Pentacene purchased from Sigma-Aldrich was purified by four cycles of gradient sublimation. We used naturally oxidized silicon wafer (SiO_2) and Cu(110) single crystal as the substrate. SiO_2 was ultrasonically cleaned in acetone and isopropanol followed by 30 minutes of ultraviolet (UV)-ozone treatment. The clean surface of Cu(110) was obtained by repeating Ar-ion sputtering and annealing cycles. Subsequently, pentacene was vacuum-deposited on the substrate at room temperature. The deposition rate and the film thickness were monitored by a quartz microbalance. During the deposition, the pressure was lower than 4.3×10^{-8} Pa. AR-LEIPS, LEIPS, and UPS measurements were performed without exposing the sample to air (in situ measurement) at room temperature and pressure lower than 4×10^{-8} Pa. For the temperature-dependent experiments, the sample was cooled by liquid nitrogen.

AR-LEIPS In AR-LEIPS measurements, the photon emitted from the sample was reflected by a concave mirror and focused on a photon detector (Figure S1). The photon detector was composed of a bandpass filter (Semrock, Inc.) and a photomultiplier tube (Hamamatsu Photonics K.K., R821). The center energy (bandwidth) of the photon detection was 4.825 eV (0.282 eV). The overall energy resolution estimated from the width of the Fermi edge of a polycrystalline Ag surface was 0.37 eV. In the angle-resolved measurements, the electron incident angle was changed between 0° and 25° by rotating the sample. As the signal accumulation took approximately four hours for each AR-LEIPS spectrum, measurement of the entire AR-LEIPS spectra required 24 hours. Meanwhile, we observed no discernible changes of the spectra due to sample damage. The sample current was 350 nA. The sample current was measured as a function of the kinetic energy of electron with the bias voltage of −5 V applied to the sample and shown as low-energy electron transmission (LEET) spectra. We smoothed the raw spectrum and computed the second derivative using the Savitzky-Golay method (the least-square fitting to 2nd order polynomial to the 15-50 data points).

Temperature-dependent LEIPS and UPS The temperature-dependent LEIPS spectra at the Γ-point were obtained in a separate LEIPS/UPS apparatus. The thickness of the film was 10 nm. Details of the experimental setup were reported elsewhere[54]. The center energy (bandwidth) of the detected photon was 4.825 eV (0.282 eV), and the overall energy resolution was 0.32 eV. Using the same apparatus, we performed UPS measurements. UPS spectra were measured with He I light (photon energy hν = 21.22 eV). The vacuum level was determined from the cutoff energy of the secondary electrons. The photoelectron energy was analyzed using a PHOIBOS-100 analyzer (SPECS). The energy resolution was approximately 100 meV, which was estimated from the Fermi edge and the secondary electron cutoff of the polycrystalline Ag film spectrum. The detection angle of the electron beam was set normal to the sample surface. The acceptance angle of the energy analyzer was set to ±3°. The second derivative were computed using the Savitzky-Golay method.

Crystal structure optimization To take the effect of van der Waal interactions on crystal structure into account, the internal atomic coordinates of the pentacene thin-film phase obtained by Yoshida *et al*.[33] were re-optimized within the framework of DFT based on the vdW-DF2 functional[37,38] The comparison of the lattice constants measured by different groups is discussed in Supplementary Information S3. For the calculation, the cutoff energies for the plane wave and the charge density were 80 and 800 Ry, respectively. The total energy convergence tolerance was set to 10^{-5} Ry. Brillouin zone integration was performed with the 4 × 4 × 4 *k*-point set. The optimized crystal structures (the lattice constants and atomic positions) are available in Yoshida_TF-PEN_vdW-DF2_300K.cif and Nabok_TF-PEN.cif as Supplementary Information.

Calculations of bare transfer integrals We evaluated bare transfer integrals t_{NM}^{0} by calculating MLWFs[39] based on DFT[37] with vdW-DF2 functional[38] The MLWFs $|W_{\alpha \boldsymbol{R}_N}\rangle$ centered on site $\boldsymbol{R}_N$ were generated from the LUMO or HOMO band states, and t_{NM}^{0} was given by $\langle W_{\alpha \boldsymbol{R}_N}|\hat{H}_{KS}|W_{\alpha \boldsymbol{R}_M}\rangle$, where α and H_{KS} represent the band index and the Kohn-Sham Hamiltonian, respectively. The cutoff energies for the plane wave and the charge density were 50 and 400 Ry, respectively. Note that the obtained

bare transfer integrals t_i^0 are good agreement with the respective transfer integrals that best fit the band structure calculated by the density functional theory (DFT) with the Perdew–Burke–Ernzerhof (PBE) exchange-correlation functional[34].

Calculation of frequency-dependent polaron coupling constant Reorganization energies λ of 129 meV for electron and 92 meV for hole were obtained by the adiabatic potential energy surface method[23] using the B3LYP/6-31G+(d,p) level derived by GAMESS[55]. The calculation was done for an isolated pentacene. In the crystal, the intermolecular interaction may have caused the increase of the reorganization energy by a factor of 1.3, as demonstrated by a high-resolution UPS experiment[56]. However, in the partially dressed polaron model, the intermolecular interaction will not affect the discussion and thus can be included as a minor correction. The reorganization energy can be decomposed into each intramolecular vibrational mode λ_l by projecting the displacement of the optimized ionic geometry (anion and cation for electron and hole, respectively) on the normal coordinates[23], as shown in Figure 3(a). The frequency of the intramolecular vibrational mode is multiplied by the scaling factor of 0.964 to better reproduce the experimental value[57]. The coupling constant is given by $g_l = \sqrt{\lambda_l / 2\hbar\omega_l}$.

Calculation of hole and electron mobilities We evaluated the electron and hole mobilities of the pentacene thin-film phase using our order-*N* quantum dynamics simulation technique called TD-WPD[51,52,58]. The charge transport properties were characterized by the interactions between the charge carriers and the molecular vibrations. The small polaron formation effect was included through the renormalization of the transfer integrals defined by Equation 3. The magnitudes of the dynamic disorder were evaluated from the changes in the transfer integrals due to the atomic displacements along the normal modes of the lattice phonons. The normal modes were obtained from the diagonalization of a dynamical matrix using force-field calculations with low computational cost[59]. We employed a monolayer consisting of 200×200 unit cells to obtain a trajectory of wave packets.

The wave packet dynamics were computed up to 500 fs with the time step of 0.5 fs. Details of the computational procedure and conditions are described in Supplementary Information S12.

REFERENCES

54. Yoshida, H. Note: Low energy inverse photoemission spectroscopy apparatus. *Rev. Sci. Instrum.* **85**, 016101 (2014).

55. Schmidt, M. W. *et al.* General atomic and molecular electronic structure system. *J. Comput. Chem.* **14**, 1347–1363 (1993).

56. Yamane, H. *et al.* Hole-vibration coupling of the highest occupied state in pentacene thin films. *Phys. Rev. B* **72**, 153412 (2005).

57. DataBase, C. C. C. and B. CCCBDB listing of precalculated vibrational scaling factors. 2015 https://cccbdb.nist.gov/vibscalejust.asp (2015).

58. Ishii, H., Kobayashi, N. & Hirose, K. Charge transport calculations by a wave-packet dynamical approach using maximally localized Wannier functions based on density functional theory: Application to high-mobility organic semiconductors. *Phys. Rev. B* **95**, 035433 (2017).

59. Goto, H., Obata, S., Nakayama, N. & Ohta, K. *CONFLEX 8*. conflex. Tokyo, Japan (2017).